

Finding black holes in numerical spacetimes

Scott A. Hughes,* Charles R. Keeton II, and Paul Walker[†]
Department of Physics, Cornell University, Ithaca, New York 14853

Kevin T. Walsh
Department of Applied and Engineering Physics, Cornell University, Ithaca, New York 14853

Stuart L. Shapiro[‡] and Saul A. Teukolsky[‡]
Center for Radiophysics and Space Research, Cornell University, Ithaca, New York 14853
 (Received 5 November 1993)

We have constructed a numerical code that finds black hole event horizons in an axisymmetric rotating spacetime. The spacetime is specified numerically by giving metric coefficients on a spatial grid for a series of time slices. The code solves the geodesic equation for light rays emitted from a suitable sample of points in the evolving spacetime. The algorithm for finding the event horizon employs the apparent horizon, which can form much later than the event horizon, to distinguish between light rays that escape to infinity and light rays that are captured. Simple geometries can be diagnosed on a workstation; more complicated cases are computationally intensive. However, the code is easily parallelized and has been efficiently run on the IBM SP-1 parallel machine. We have illustrated the use of the event horizon code on two cases. One is the head-on collision of two black holes that form from the collapse of collisionless matter, coalescing to a single Schwarzschild black hole. The other is the collapse of a rotating toroid to form a Kerr black hole. In this case the horizon initially appears with a toroidal topology. This is the first known example of this phenomenon.

PACS number(s): 04.25.Dm, 97.60.Lf

I. INTRODUCTION

A major effort is underway to develop computer codes that can solve Einstein's equations of general relativity for physically realistic systems. The spherical problem, where the field is nondynamical and no gravitational waves are produced, is essentially solved. Current work focuses on multidimensional systems with dynamical gravitational fields.

Some of the most interesting questions in numerical relativity concern the formation of black holes from gravitational collapse or collisions. A curious paradox, however, is that the appearance and growth of a black hole cannot be determined in a numerical simulation until after the complete spacetime has been constructed. The reason is that there is no instantaneous criterion for deciding whether a particular event is inside or outside a black hole. Rather, it is necessary to determine the fate of all possible light rays emitted from that event. If any light ray can escape to infinity, the event is outside the black hole. If no light ray can reach infinity, the event is inside the black hole.

The *event horizon*, or surface of the black hole, is the boundary between events that can send light rays to infinity and those that cannot. Thus light rays have to be tracked arbitrarily far into the future to identify this boundary. As one evolves a spacetime numerically from one time slice to the next, it is thus impossible to locate the surface of the black hole on each slice concurrently. One must go back after one has determined the fate of light rays to mark the event horizon on any given slice.

In some cases, an *apparent horizon* signals the existence of a black hole. An apparent horizon is also determined by the fate of beams of light, but in this case it is the instantaneous fate of the rays that counts. In a weak gravitational field about a central source, an outward beam of light diverges, and its cross-sectional area increases. However, a sufficiently strong gravitational field actually focuses the light so that the area of the beam immediately decreases. Such a strong field defines a region of closed trapped surfaces, from which all outgoing beams of light converge. The apparent horizon is the outer boundary of the region of closed trapped surfaces. If an apparent horizon is present on any given time slice, then there must be a black hole on that slice, and the apparent horizon must lie inside the hole's event horizon [1]. At late times, when the gravitational field has settled down to a stationary state, the event horizon and the apparent horizon coincide.

An apparent horizon is readily identified from the computed metric on each time slice as it is produced in a numerical code. While its appearance guarantees the presence of a black hole, there are two problems with us-

*Present address: Department of Physics, California Institute of Technology, Pasadena, CA 91125.

[†]Present address: Department of Physics, University of Illinois at Urbana-Champaign, Urbana, IL 61801.

[‡]Also at Departments of Astronomy and Physics, Cornell University, Ithaca, NY 14853.

ing an apparent horizon as a diagnostic for black holes. First, a black hole may be present on the slice without an apparent horizon. Second, even when the apparent horizon exists, the event horizon does not coincide with it, especially in the early stages of black hole formation.

In this paper we present a code that maps out the event horizon given a numerical spacetime and the apparent horizon. It takes an input numerically generated metric coefficients for an axisymmetric spacetime and probes the geometry using null geodesics. We employ a simple criterion to decide for a simulation that lasts only a finite time whether a light ray emitted from a given point in spacetime is “captured” or “escapes.” We apply the criterion to a large number of points in the numerical spacetime, and thereby locate the event horizon. We illustrate the technique on some examples involving collisions and collapses of relativistic objects.

II. NUMERICAL TECHNIQUE

A. Tracking the paths of light rays

The code takes as input numerical metric coefficients for an axisymmetric line element in Arnowitt-Deser-Mizner (ADM) 3+1 form. The spatial part of the metric γ_{ij} in the quasi-isotropic gauge is

$${}^{(3)}ds^2 = \gamma_{ij} dx^i dx^j = A^2(dr^2 + r^2 d\theta^2) + B^2 r^2 (\xi d\theta + \sin\theta d\phi)^2. \quad (1)$$

The remaining parts of the metric are constructed using the spatial metric γ_{ij} , the lapse function α , and the shift vector β^i :

$$g_{00} = -\alpha^2 + \gamma_{ij} \beta^i \beta^j, \quad (2)$$

$$g_{0j} = \gamma_{ij} \beta^i.$$

For nonrotating matter, $\xi=0$, $\beta^\phi=0$. Although the software is written to accept data in the quasi-isotropic gauge of Eq. (1), it is trivial to modify it for other gauge choices.

The core of the event horizon software is a numerical routine for solving the geodesic equation for light rays. Recall that the geodesic equation is

$$\frac{d^2 x^\mu}{d\lambda^2} + \Gamma_{\alpha\beta}^\mu \frac{dx^\alpha}{d\lambda} \frac{dx^\beta}{d\lambda} = 0, \quad (3)$$

where λ is an affine parameter. The photon four-momentum \mathbf{p} has components

$$p^i = \frac{dx^i}{d\lambda}, \quad (4)$$

$$p^0 = \frac{1}{\alpha} \sqrt{\gamma^{ij} p_i p_j},$$

where the expression for p^0 enforces $\mathbf{p} \cdot \mathbf{p} = 0$. Using the 3+1 form of the metric and Eq. (4), we write the geodesic equation as two coupled first-order equations:

$$\frac{dp_i}{d\lambda} = -\alpha \alpha_{,i} (p^0)^2 + \beta^k_{,i} p_k p^0 - \frac{1}{2} \gamma^{lm}_{,i} p_l p_m, \quad (5)$$

$$\frac{dx^j}{d\lambda} = \gamma^{ij} p_i - \beta^j p^0. \quad (6)$$

Given an initial photon position and momentum, together with a metric, Eqs. (5) and (6) can be integrated to find the photon trajectory.

The code is designed to receive a numerical metric on a spatial grid on successive time slices. The grid consists of radial and angular meshes that can vary from time step to time step.

The equations are integrated with a fourth-order Runge-Kutta method with variable step size and fifth-order error estimation [2]. To integrate the geodesic equations we need to know the values of the fields and the field derivatives at each point in spacetime along a null ray. Thus, we need to differentiate the fields numerically, and interpolate the field values and derivative values to a point that is not necessarily a mesh point. Derivatives at the midpoints of a grid zone are computed by first-order differencing and then bilinearly interpolated onto the original mesh points. This scheme becomes second-order accurate in the limit of uniformly spaced grid points. Note that the geodesic equations require only first derivatives.

We use the regularity of the various fields near the origin and axis to improve the accuracy of the differencing. For example, the metric function A varies like [constant + $\mathcal{O}(r^2)$] near the origin. Thus we write the radial derivative as

$$A_{,r} = 2r A_{,r^2} \quad (7)$$

and difference it as

$$(A_{,r})_{i+1/2} = 2r_{i+1/2} \frac{A_{i+1} - A_i}{r_{i+1}^2 - r_i^2}. \quad (8)$$

In following a light ray, the Runge-Kutta integrator requires field values at spacetime points that do not lie on the stored mesh points. These are computed by trilinear interpolation in the variables r , $\cos\theta$, and t from the mesh points to the point on the null ray. All of our cases are axisymmetric, so ϕ is ignorable. Once again, to improve accuracy we consider the regularity of the fields when interpolating. For example, we interpolate A linearly in r^2 , rather than in r .

Our code can run on a workstation-class machine with a graphical user interface, so we can actually watch light rays be integrated with manually chosen initial conditions. However, the complete file of metric data for a typical case is too large to fit into the memory of a workstation. For example, the case described in Sec. IV B below has seven metric variables on a 201 radial by 17 angular grid for 240 time slices. These data require about 60 Mb of storage. To accommodate the memory resources of workstations, we leave the metric file on disk and do fast indexed searches of the disk file. We read in only the local grid and metric information necessary for the current integration path. Hence the code runs on a machine with small internal memory (less than 3 Mb) but in this case is limited computationally by disk access speed. However, the code runs very effectively on a

parallel machine in which each node has its own local disk, such as Cornell's IBM SP-1, which was used to probe rotating spacetimes (see Sec. IV B).

B. Using light rays to locate event horizons

We need a criterion to decide whether a light ray propagating in a spacetime that has been constructed for only a finite time ultimately escapes or is captured. We experimented with a number of different strategies. An obvious choice is to examine the slope of the null geodesic at the last time slice to decide whether the ray is ingoing or outgoing. In practice, however, this test is not very effective unless the simulation has proceeded to very late times and the geometry has become nearly stationary. A more reliable criterion takes advantage of the appearance of an apparent horizon at late times. If at any time a light ray passes into an apparent horizon, we know with certainty that it is within an event horizon and has been captured by a black hole. If all light rays launched from a point in spacetime, regardless of initial momentum, are captured in this manner, then that point in spacetime is inside the black hole. If at least one light ray is not captured but instead "escapes," the point is not inside the black hole.

The surface separating these "escape" or "capture" points is the event horizon of the black hole. There are two possible sources of error in our calculation of this surface. First, our estimate is conservative; technically, one must follow a light ray for an infinite time to decide whether or not it is captured. We have only a finite span of data; light rays that we label "escape" may in fact move into the apparent horizon after the simulation has ended. Thus, the event horizons we calculate could be smaller than the "true" event horizons. However, this effect is minimized whenever the simulation proceeds far enough that the apparent horizon area has grown to the stationary Schwarzschild or Kerr value. We assume that at this point the apparent and event horizons coincide, and our plots automatically reflect this.

A second possible source of error arises from the finite number of light rays that can be launched from a point. It is possible that there exists some unexamined direction that allows light rays to escape. Thus, in principle some of our "capture" points may be "escape" points, so that our estimate of the event horizon size could be too large. To rule out this latter source of error, we experimented with increasing numbers of photon directions from each point. For nonrotating spacetimes, where the null path $r=r(\theta)$ is independent of p_ϕ , we found that 48 photon launches per point was always adequate to specify the event horizon at the resolution of a graphical image. For these spacetimes we integrate $N=48$ light rays with $p_\phi=0$, and the other two components varied uniformly over the momentum space unit circle:

$$\begin{aligned} (p_{\hat{r}})_j &= \cos \left[\frac{2\pi j}{N} \right], \\ (p_{\hat{\theta}})_j &= \sin \left[\frac{2\pi j}{N} \right], \quad j=0, \dots, N-1. \end{aligned} \quad (9)$$

In axisymmetric, rotating spacetimes, varying p_ϕ can have significant dynamical consequences. For example, in the Kerr spacetime counterrotating tangential light rays fall into the black hole from a larger initial radius than corotating tangential light rays. So now we must include light rays with nonzero p_ϕ in our choice of null directions. This extra degree of freedom requires a larger number of light rays. In practice we launch about $N=750$ light rays from each point in rotating spacetimes.

We implement our algorithm for finding the event horizon at a given time in two stages. First, we find a rough approximation to the event horizon. Using the approximation as a starting point in searching for the actual event horizon allows us to reduce the number of spacetime points we must examine. The most efficient way of determining the approximate event horizon on any given time slice is to adopt the already-determined event horizon on a nearby time slice as our approximation. When we first start up the code to look for the event horizon, we know the location of the event horizon on the *last* time slice, since by assumption it coincides with the apparent horizon then. We therefore adopt the strategy of locating the event horizon on successive slices moving *backwards* in the spacetime, thereby always having a good approximation available.

Stage two consists of refining our approximation to produce an accurate event horizon. First, we launch rays from a given point on the approximate horizon. If the point is inside the black hole, then the event horizon is larger than the approximate horizon, so we step outward along the vector normal to the approximate surface; if the point is outside the black hole, the event horizon is smaller than the approximate horizon, so we step inward along the normal vector. We then launch another set of rays from the new point, and step accordingly. When we find two consecutive points, one of which is inside and one outside, we bisect the interval and continue testing until we find two points whose coordinates are less than some ϵ apart. In practice we have used $\epsilon/M=10^{-3}$.

III. TEST CALCULATIONS

To test our code, we studied light rays and the horizon structure in four well-understood spacetimes: flat space in spherical polar coordinates, the Schwarzschild exterior and interior geometry in Kruskal-Szekeres coordinates [3], exterior Kerr in Boyer-Lindquist coordinates [3], and Oppenheimer-Snyder collapse in maximal slicing and isotropic coordinates [4].

Photons in flat spacetime travel in straight lines. The major source of numerical difficulty here is that in polar coordinates the geodesic equations have coordinate singularities on the z axis ($\theta=0, \pi$) and at the origin ($r=0$). Trajectories sufficiently close to the axis were continued across the axis by setting $\phi \rightarrow \phi + \pi$; trajectories close to the origin require setting $\theta \rightarrow \pi - \theta$ as well. Together with the regularized differencing and interpolation described in Sec. II we were then able to handle these singularities with no difficulty.

For our next test we studied the behavior of light rays in the Schwarzschild geometry using Kruskal-Szekeres

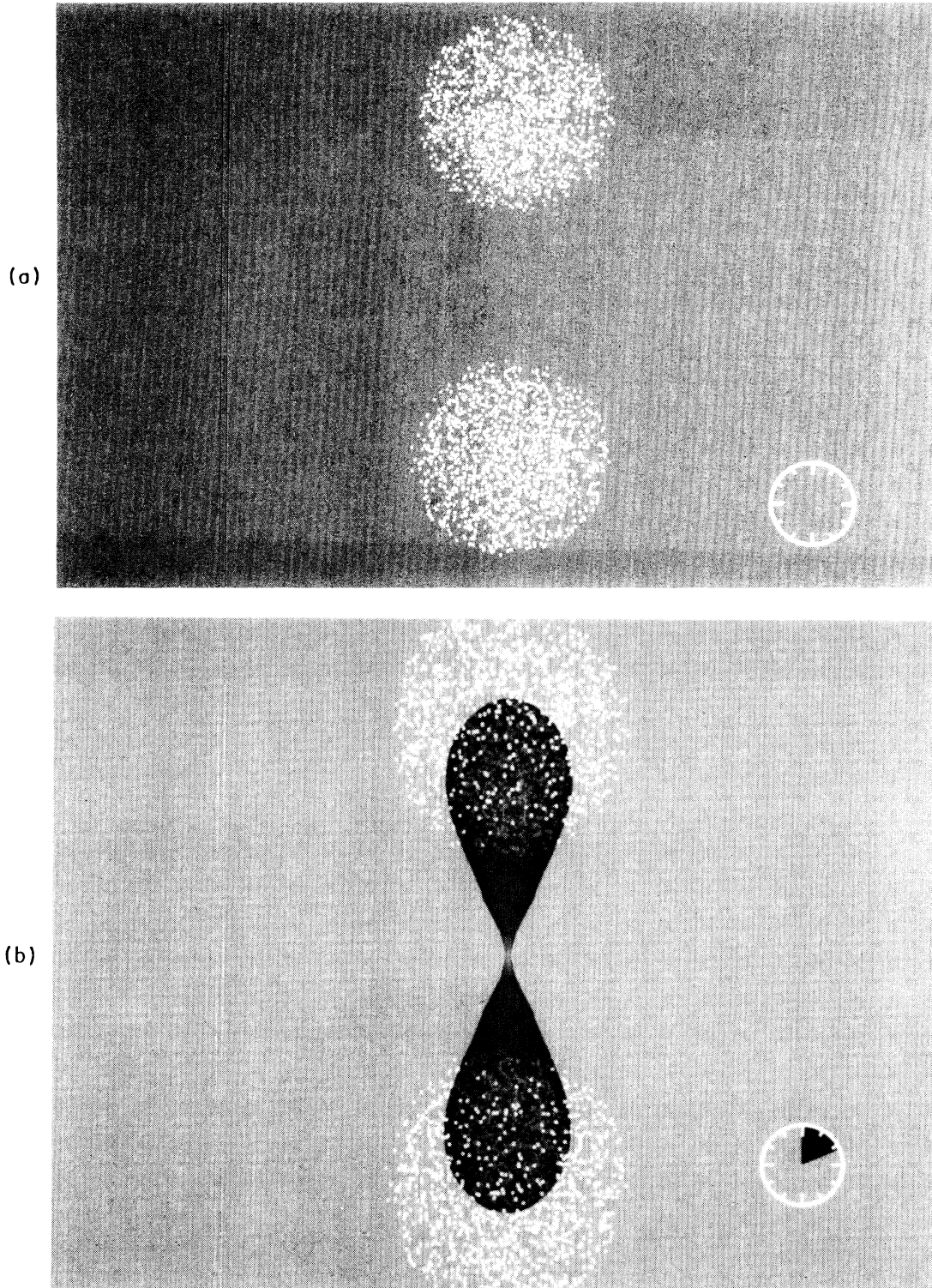
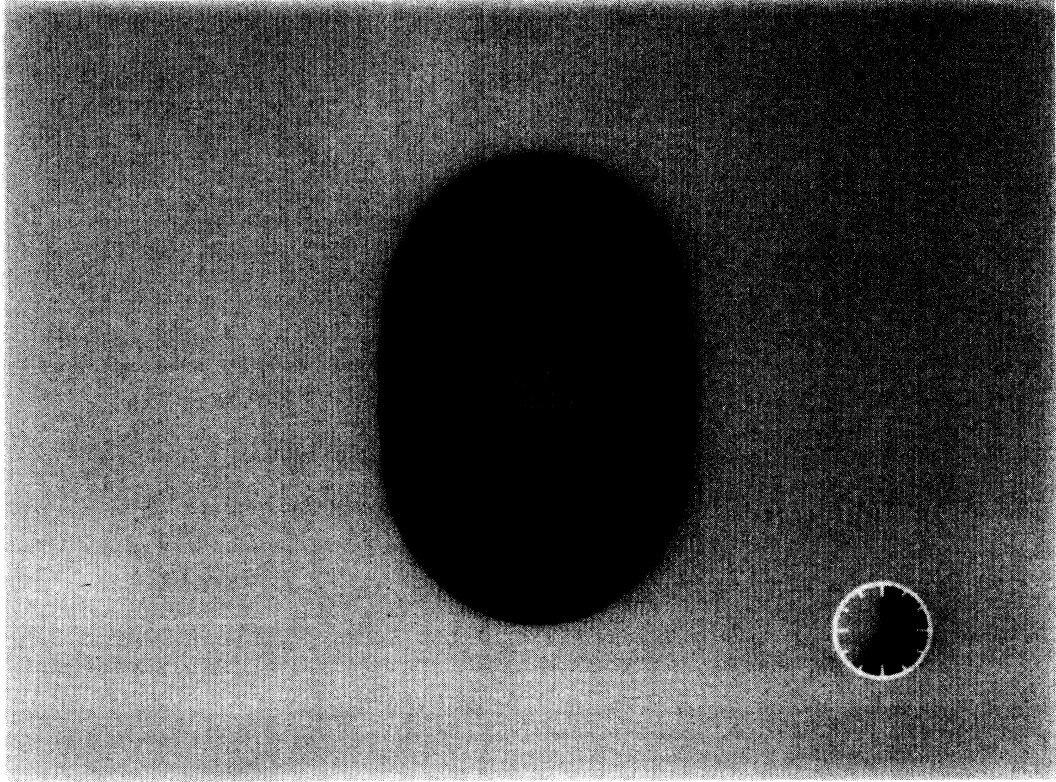


FIG. 1. Three-dimensional views of the head-on collision of boosted spherical clusters [5]. (a) Initial data. Each sphere has an initial radius $a/M=0.8$, an inward boost velocity $v=0.15$, and their centers are at $z_0/M=\pm 1.4$. Sample particles from the collisionless matter distribution are represented by white dots. A clock displaying the elapsed fraction of the total evolution time appears in the corner. (b) Horizon coalescence. At time $t/M=2.18$, the two event horizons coalesce (shaded hourglass). The clusters' centers are at $z/M=\pm 1.07$. The scale of the image has been enlarged by about a factor of 2 from that of (a). (c) Appearance of apparent horizons. At time $t/M \simeq 6.5$, the common apparent horizon appears, well inside the event horizon. At time $t/M \simeq 7.1$ (shown here), the disjoint apparent horizons appear. The outer shaded region denotes the event horizon, the darker shaded region just inside is the common apparent horizon, and the two darkest regions are the disjoint apparent horizons. (d) Final state. The event and common apparent horizons have settled down to a quasistationary state and coincide. At time $t/M \simeq 11.7$ shown here, the area is $\mathcal{A}/16\pi M^2=1.1$, the polar circumference is $\mathcal{C}_{\text{pole}}/4\pi M=1.1$, and the equatorial circumference is $\mathcal{C}_{\text{eq}}/4\pi M=1.0$.

(c)



(d)

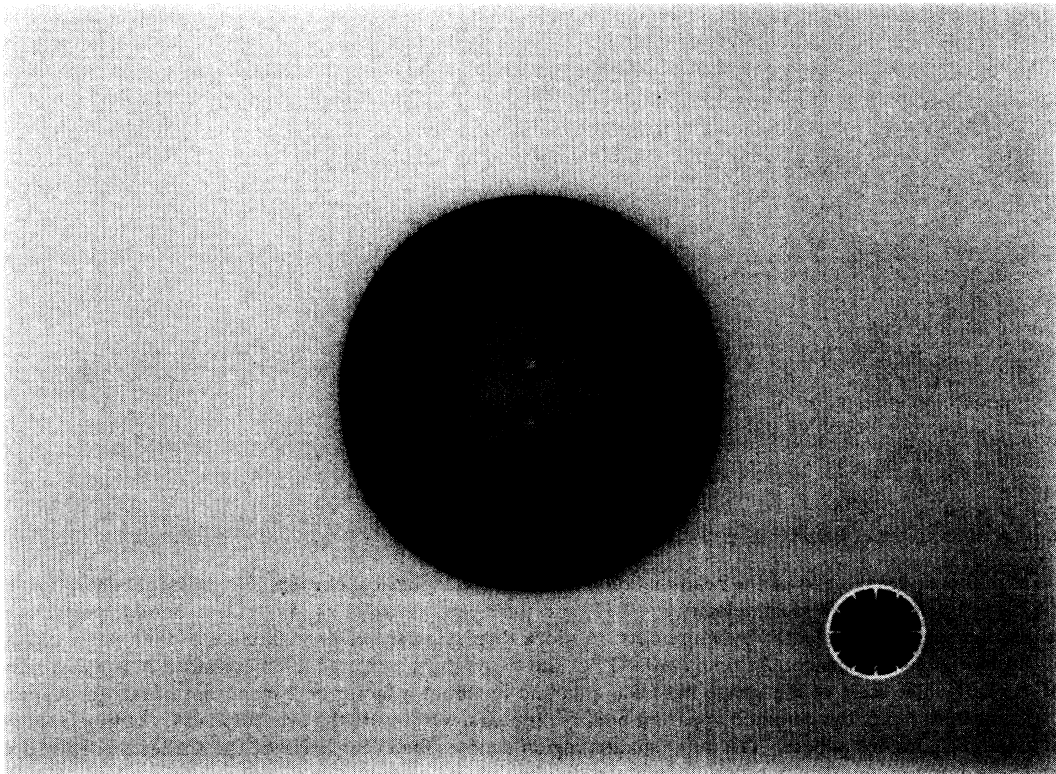


FIG. 1. (*Continued*).

coordinates [3]; recall that the line element in these coordinates is

$$ds^2 = \left[\frac{32M^3}{r} \right] e^{-r/2M} (-dv^2 + du^2) + r^2 d\Omega^2. \quad (10)$$

Kruskal-Szekeres coordinates are extremely useful as a check because light rays, especially radial light rays, exhibit simple behavior: As can be seen from the line element (10), all radial light rays satisfy the equation $u = \pm v + \text{const}$. We first allowed the code to evaluate the analytic expressions for both the Kruskal-Szekeres metric functions and their derivatives along light rays. We found that radial light rays traveled along 45° trajectories in (u, v) space as they should. We also were able to keep a photon in an orbit at $r = 3M$ for many periods. We next evaluated the metric functions alone analytically and inserted their values on grid points into the code. We then reran the simulation, thereby testing the interpolation and numerical derivative routines. Our results were virtually identical: radial light rays again moved along precise 45° trajectories, and we found an unstable orbit very close to $r = 3M$. We were also able to locate the event horizon at $r = 2M$ to better than a part in 10^4 .

We next studied the exterior Kerr geometry in Boyer-Lindquist coordinates. We focused on finding the location of the unstable photon orbits in the equatorial plane for various values of a , since analytic expressions exist for the locations of these orbits [3]. The grid we used consisted of 301 radial grid points evenly spaced between the Kerr event horizon, $M + \sqrt{M^2 - a^2}$, and $10M$; it used 21 angular grid points evenly spaced in $\cos\theta$. For all values of a that we tested, we were able to identify the location of critical orbits to a part in 3000.

The final test treated Oppenheimer-Snyder collapse, a simple analytic spacetime with an event horizon that grows with time. We used the metric in maximal time-slicing and isotropic coordinates derived by Petrich *et al.* [4] and followed the collapse of a sphere with an initial areal radius of $10M$. This metric was placed on a numerical grid consisting of 155 radial grid points in the matter interior and 101 radial grid points in the matter exterior. Our goal in this test was to locate the time evolving event horizon. We supplied the code with information about the apparent horizon (a spherical surface of areal radius $r = 2M$ that first appears at $t = 45M$). We used the code to map out the event horizon and found good agreement with the results of Ref. [4]. For example, we found that the event horizon first appears at the origin at $t = 38.43M$, which compares well with the value $t = 38.4117M$ quoted in Ref. [4].

IV. RESULTS

A. Head-on collision of two black holes

As one application of our code, we studied the event horizons that form during the collision of boosted spheres

of particles. The particles are assumed to obey the relativistic collisionless Boltzmann equation (Vlasov equation); the evolution is simulated with an axisymmetric evolution code and the solution is described in Ref. [5]. We regenerated the solution using 250 radial zones and 32 angular zones, taking about 3.6 CPU hours on the IBM ES9000 supercomputer. We took the metric and apparent horizons produced by the evolution code as input for our event horizon finding code.

As described in [5], the spheres each have an initial radius $a = 0.8M$ and are centered at $z_0 = \pm 1.4M$. There are no apparent horizons initially. The nonequilibrium spheres are boosted toward each other, imploding on their own centers while approaching each other head-on. By suitable choice of parameters, we can treat the head-on collision of two black holes in this manner.

We chose the spheres to have an inward boost velocity of $v = 0.15$ as measured by the normal observer (an observer whose four-velocity is normal to the $t = 0$ initial time slice). The evolution code found a common apparent horizon appearing at $t \approx 6.5M$ and disjoint horizons appearing at $t \approx 7.1M$. The horizon code found event horizons appearing much earlier than the apparent horizons. In particular, we found disjoint event horizons appearing within the spheres of matter as early as $t \approx 0.13M$.

The disjoint event horizons are tidally distorted, growing toward each other until they coalesce at $t \approx 2.16M$, forming a single event horizon (Fig. 1). The single event horizon expands along the equator and contracts along the axis. At time $t \approx 6.5M$ the common apparent horizon appears, well within the event horizon. At time $t \approx 7.1M$ the disjoint apparent horizons appear. We terminate the evolution at $t \approx 11.7M$.

In Fig. 2 we show cross sections of the collision in a meridional plane. In the first snapshot, the event horizon has formed in the interior of each of the spheres but has not yet coalesced. Coalescence first takes place in the second snapshot. The last three snapshots in Fig. 2 are at the same times as the last three in Fig. 1.

In Fig. 3 we show the spacetime diagram for this collision. The formation of the common and disjoint apparent horizons at $t \approx 6.5M$ and $t \approx 7.1M$, respectively, is seen as the sudden appearance of a dark surface within the event horizon. This picture is an actual calculation of the schematic diagrams first sketched over 20 years ago [6].

Figure 4 displays the trajectories of outward radial light rays launched from the axis at $t = 4M$. The dashed line is the event horizon found by our code. From the plot, it is clear that light rays initially inside the event horizon move further within the horizon, while light rays initially outside the event horizon move further out. This behavior increases our confidence in the surface we find.

In Fig. 5 we plot the area of the event horizon. We normalize the area to that of the expected final state, a single Schwarzschild black hole of mass M . We take M to be the initial total mass energy, since the energy carried off by gravitational waves is small [5]. When the two event horizons coalesce, their total area is $\mathcal{A}/16\pi M^2 = 0.48$. When the common apparent horizon

appears, the area of the event horizon is $\mathcal{A}/16\pi M^2=0.99$, while the area of the common apparent horizon is $\mathcal{A}/16\pi M^2=0.85$. Both areas grow monotonically, settling down together to a value close to unity. By the end of the simulation, the area of both horizons is $\mathcal{A}/16\pi M^2=1.1$. According to the area theorem, the area must grow monotonically and asymptote to 1 when the radiation is small. The 10% discrepancy that we find at late times is due to numerical inaccuracies in following the late time behavior of the black hole with the evolution code as the central singularity develops.

B. Collapse of rotating toroids

We have also studied event horizons that form during the collapse of rotating toroidal configurations of col-

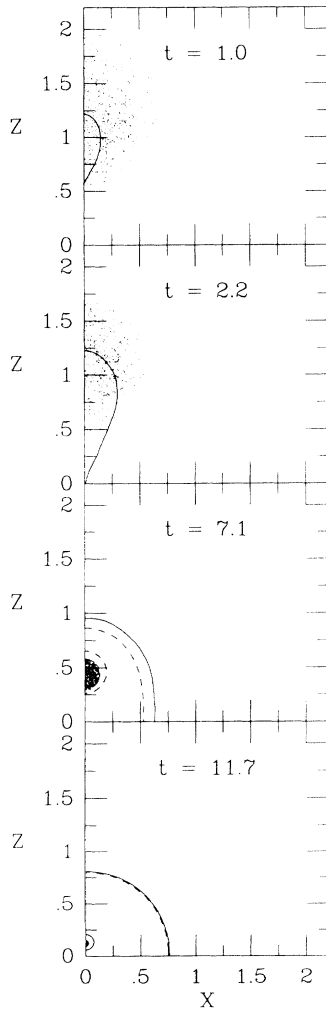


FIG. 2. Snapshots at selected times for the collision shown in Fig. 1. The solid line denotes the event horizon, and the dashed lines the common and disjoint apparent horizons. The last three snapshots are at the same times as the last three images in Fig. 1. t , x , and z are in units of M .

lisionless matter. The initial data used to generate the equilibrium clusters and the rotating evolution code used to evolve the clusters are described in Ref. [7]. We regenerated the solution using 200 radial zones and 16 angular zones. This run took about 8 CPU hours on the IBM ES9000. Again, the metric and apparent horizons produced by the evolution code provide the input for the event horizon finding code.

Here we present the results for case 10 of Ref. [7]. The cluster in that case is based on a solution for a rotating toroidal cluster in stable equilibrium. The cluster has an outer circumferential radius of $R_o/M=4.5$. In order for the cluster to collapse, it is necessary to modify it away from equilibrium. To accomplish this, we cut down the angular momentum of each particle by a factor of 0.5, producing a nonequilibrium cluster with total angular momentum $J/M^2=0.70$. The toroid initially collapses along its minor radius to a thin hoop; then, while undergoing oscillations along the minor radius, it collapses inwards along the major radius. The matter and the horizons are plotted in Fig. 6.

As discussed in Sec. II B, exploring the geometry of a rotating spacetime requires integrating many more light rays than required for a nonrotating spacetime. We generally integrated 750 light rays per point in the rotating case, except near the origin where we sometimes needed 3000 light rays to get accurate results. Integrating this many light rays took far too long to run on a serial computer. We therefore modified the event horizon finding code to perform parallel computation using the IBM SP-1 parallel supercomputer, which consists of RS-6000 class CPU's. The code is very easy to parallelize because each light ray moves independently in the same predetermined spacetime metric. Using 16 processors gave essentially a 16-fold speedup over the serial version. Generating the event horizon for the toroidal case took approximately 30 CPU hours per processor on the SP-1.

As in the collision case, we found that the event horizon appears much earlier than the apparent horizon (Figs. 6 and 7). The topology of the event horizon is rather remarkable: it initially develops as a toroid, beginning at $t \approx 13.2M$. It first forms entirely within the vacuum, between the origin and the inner edge of the toroidal cluster. The toroidal event horizon expands along its minor axis until the central hole of the doughnut pinches off at $t \approx 13.5M$. This time at which the horizon becomes topologically spherical is approximately when the outer edge of the event horizon reaches the inner edge of the toroid of matter. The event horizon expands along the axis, and the apparent horizon appears inside it at $t \approx 18.0M$. By the time we terminate the evolution at $t \approx 23.2M$, the event horizon and the apparent horizon have settled down to a quasistationary state.

Figure 8 shows the evolution of the area of the event and apparent horizons. The black hole approaches a Kerr black hole, so we have normalized the areas to the Kerr value

$$\mathcal{A}_{\text{Kerr}} = 8\pi M [M + \sqrt{M^2 - a^2}], \quad (11)$$

(where $a = J/M$). When the toroidal event horizon be-

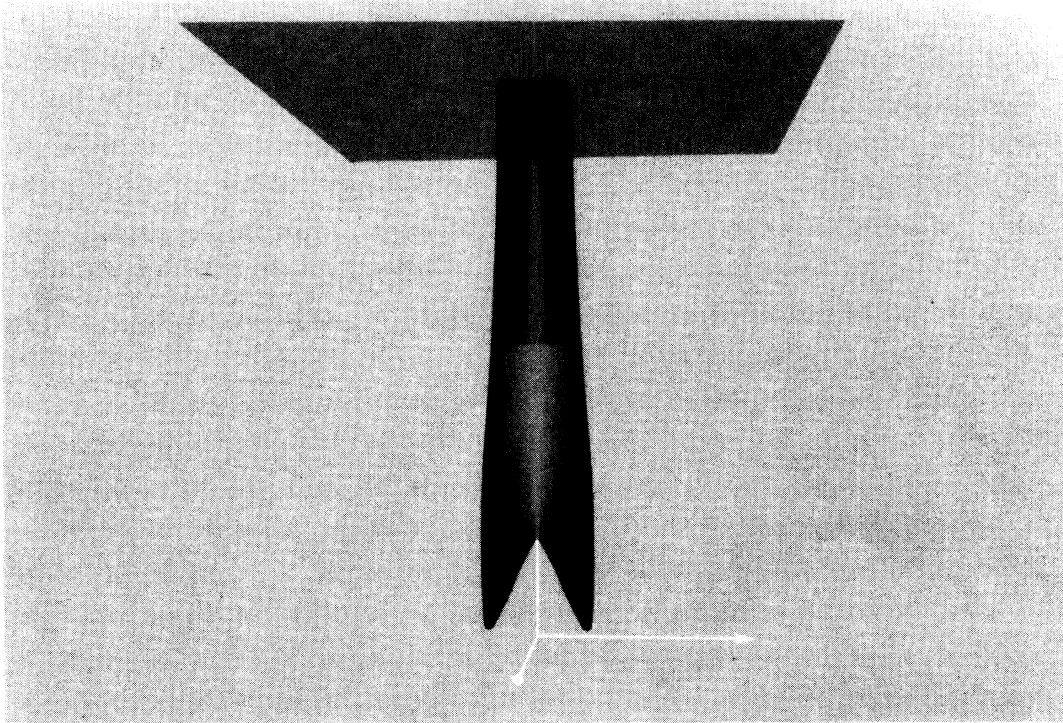


FIG. 3. Spacetime diagram for the collision depicted in Fig. 1. The time axis is vertical, the z axis (symmetry axis) points to the right, while the x axis (equatorial axis) points out of the page. The formation of the common and disjoint apparent horizons at $t/M \approx 6.5$ and 7.1 , respectively, is seen as the sudden appearance of darker surfaces inside the event horizon (outermost shaded surface). The final hypersurface $t/M \approx 11.7$ is shown as the plane at the top.

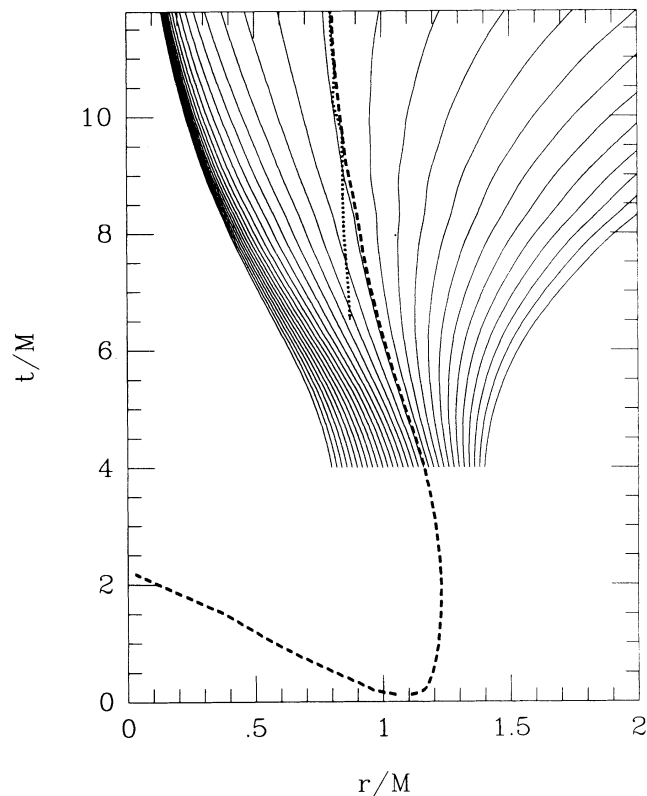


FIG. 4. Trajectories of outward radial light rays launched from the axis at $t/M = 4$ for the collision depicted in Fig. 1. The dashed line indicates the event horizon located by our code. Light rays initially inside the event horizon remain within the event horizon, while light rays initially outside diverge and remain outside. The dotted line denotes the apparent horizon.

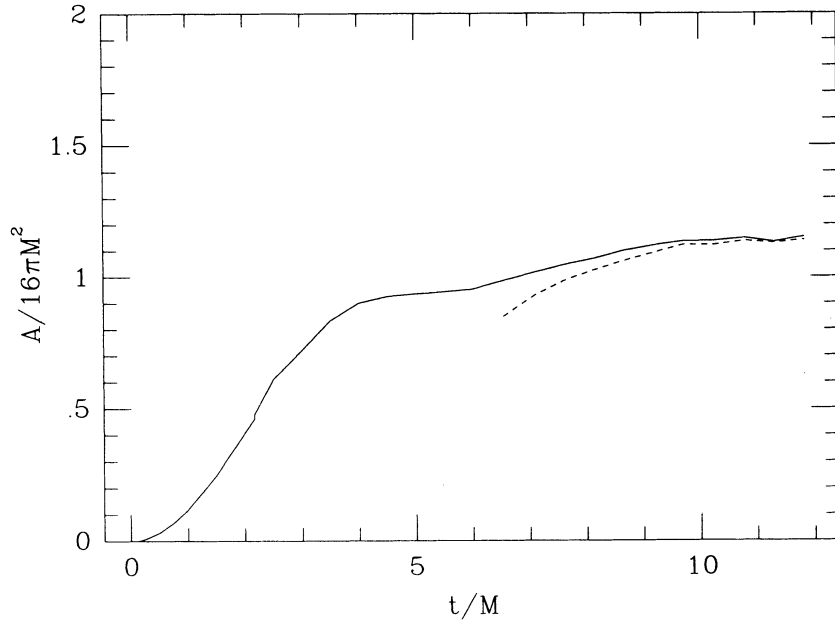


FIG. 5. Growth of the horizon area for the collision depicted in Fig. 1. The area is normalized to the Schwarzschild value $16\pi M^2$, where M is the initial total mass. The solid line is for the total area of the event horizon, the dashed line for the common apparent horizon.

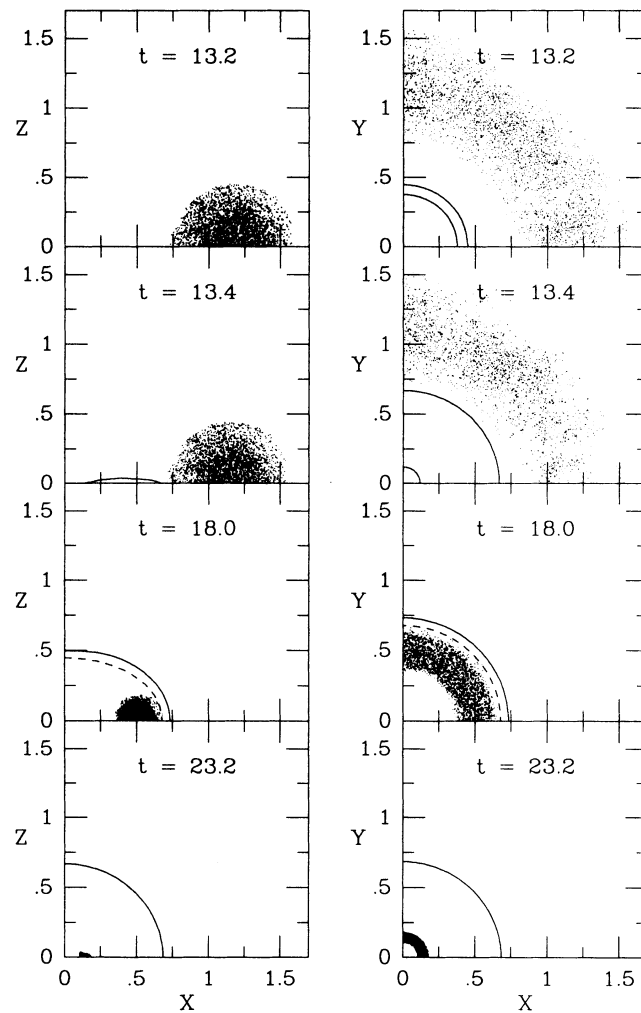


FIG. 6. Snapshots at selected times of the collapse of a rotating toroid of collisionless matter (case 10 of Ref. [7]). The left panel displays meridional slices, the right panel shows the equatorial plane. The solid line denotes the event horizon, the dashed line the apparent horizon. The earliest times shown are soon after the toroidal event horizon appears. By the final time shown, the event and apparent horizons coincide. t , x , y , and z are in units of M .

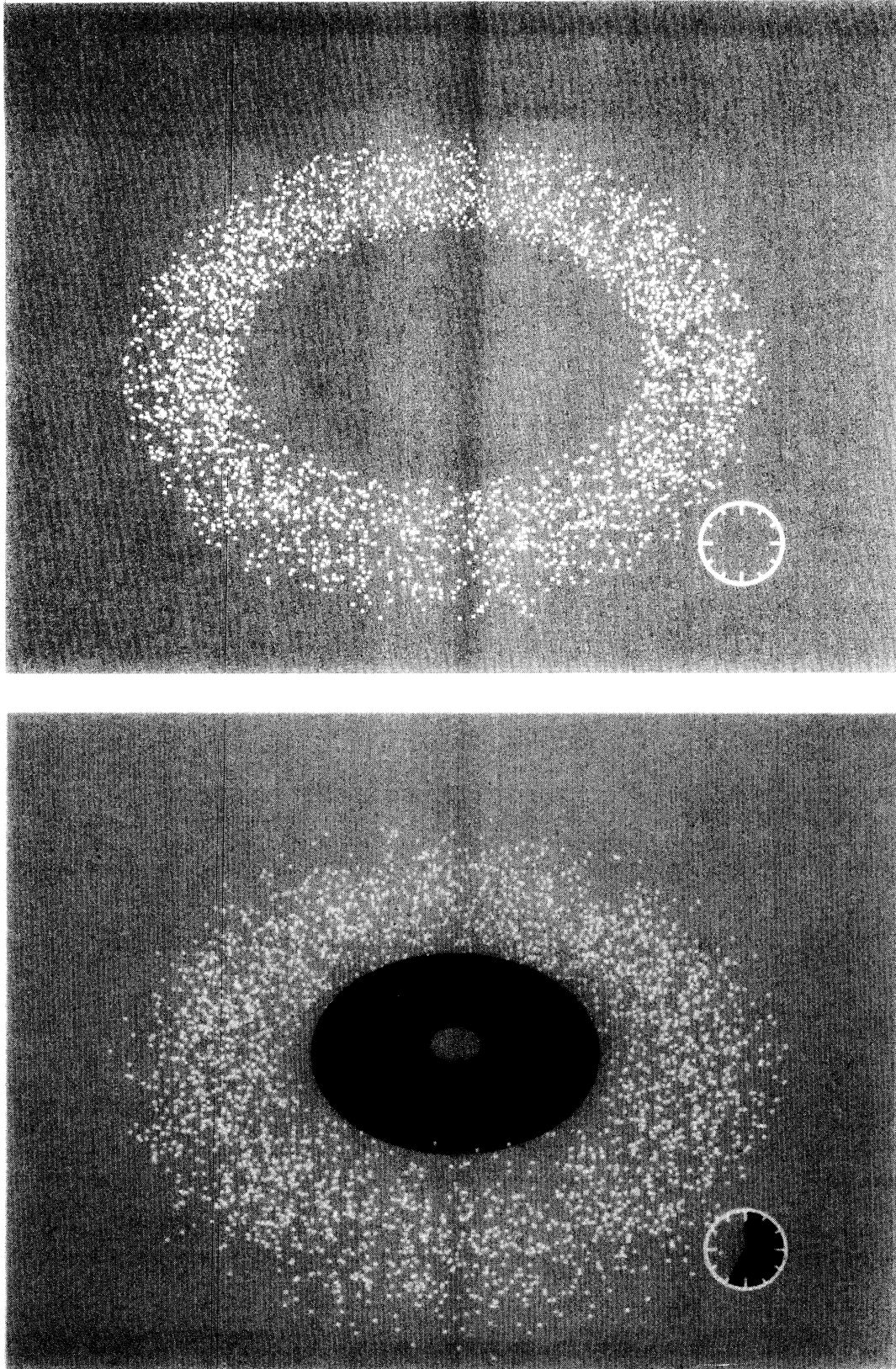


FIG. 7. Three-dimensional views of the collapse of the rotating toroid depicted in Fig. 6. The images are viewed from 45° above the equatorial plane. The first image shows the initial configuration, while the remaining three images are at the same times as the last three images of Fig. 6. The outermost shaded region is the event horizon, the shaded region inside it is the apparent horizon. The scale of the last three images has been enlarged by about a factor of 2 over the first image.

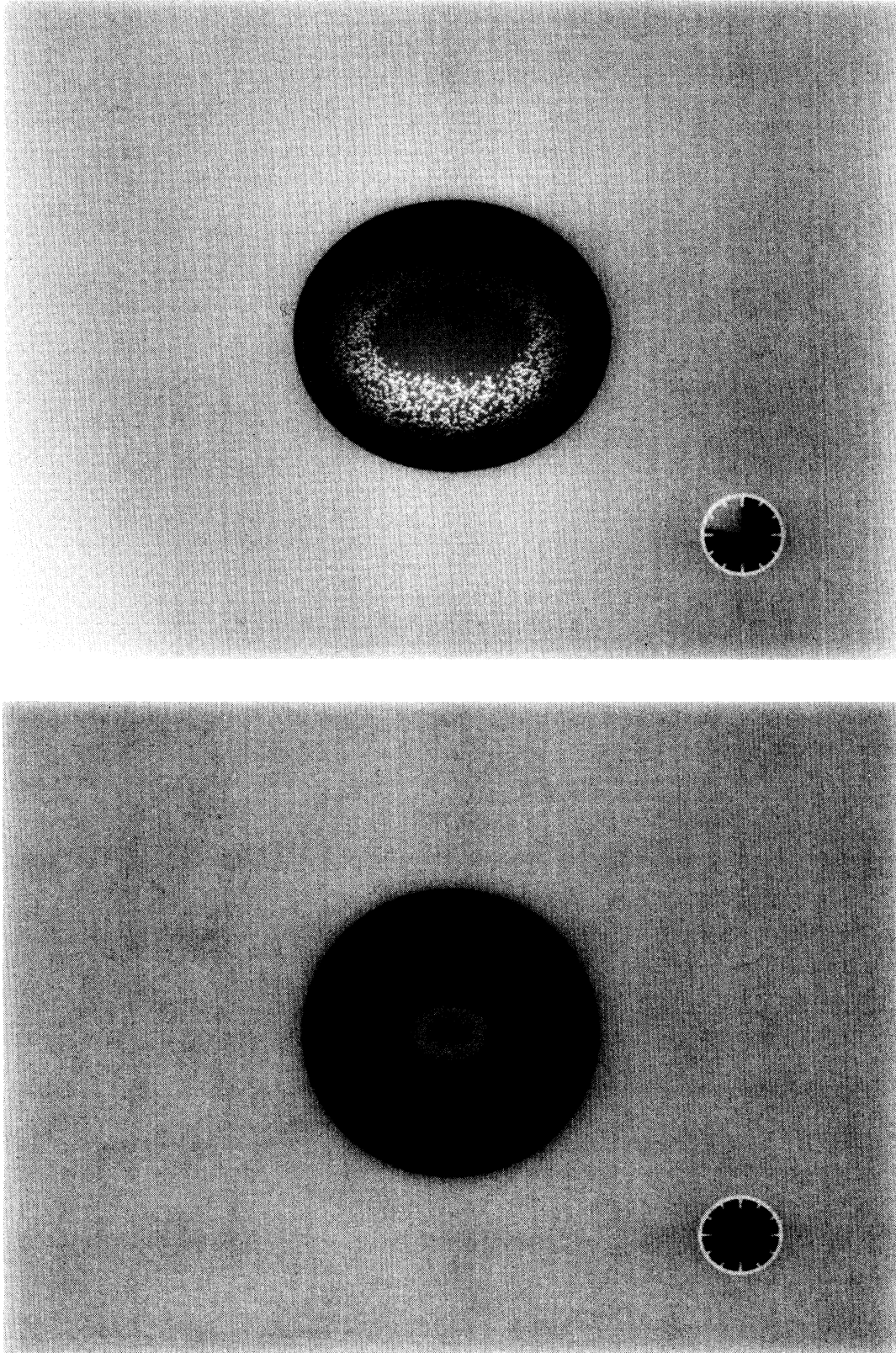


FIG. 7. (Continued).

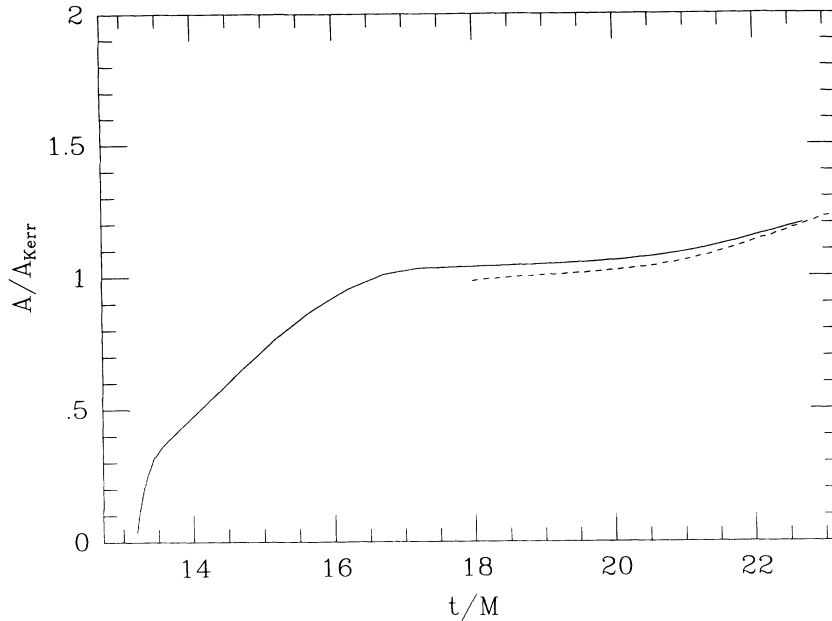


FIG. 8. Growth of the horizon area for the toroidal collapse depicted in Fig. 6. The area is normalized to the Kerr value, Eq. (11). The solid line is for the area of the event horizon, the dashed line for the apparent horizon.

comes topologically spherical, its area is $\mathcal{A}/\mathcal{A}_{\text{Kerr}}=0.33$. When the apparent horizon appears, the area of the event horizon is $\mathcal{A}/\mathcal{A}_{\text{Kerr}}=1.04$, while the area of the apparent horizon is $\mathcal{A}/\mathcal{A}_{\text{Kerr}}=0.98$. At the end of the simulation, the area of both horizons is $\mathcal{A}/\mathcal{A}_{\text{Kerr}}=1.2$. As in the colliding case, the deviation of this ratio from unity at late times is due to numerical error in the evolution code. Note that the ratio remains roughly constant near unity for a duration of many M , showing the approach to a stationary state.

Though the event horizon is toroidal for only a small amount of time during the evolution, about $0.3M$, we believe we have enough spatial and temporal resolution in the data to be confident of the toroidal geometry. We are not aware of any other examples of toroidal event horizons being reported before. We ran the same toroidal collapse case reported here, but with equal numbers of co- and counterrotating particles (case of Ref. [7]). We found a horizon with spherical topology at all times.

Presumably, toroidal horizons can occur only in spacetimes with rotation.

ACKNOWLEDGMENTS

We thank Michael Blanton and Michael Chia for assistance with visualization and for help developing the horizon finder algorithm. We also thank Andrew Abrahams for useful discussions and Michael Piper for programming assistance in the early stages of the project. S.H., C.K, P.W., and K.W. were supported in part by the Research Experiences for Undergraduates program of the National Science Foundation. This research was supported in part by NSF Grants Nos. AST 91-19475 and PHY 90-07834 and NASA grant NAGW-2364 at Cornell University. Computations were performed at the Cornell Center for Theory and Simulation in Science and Engineering, which is supported in part by the National Science Foundation, IBM Corporation, New York State, and the Cornell Research Institute.

-
- [1] S. W. Hawking and G. F. R. Ellis, *The Large Scale Structure of Space-Time* (Cambridge University Press, Cambridge, 1973).
- [2] W. H. Press, S. A. Teukolsky, W. T. Vetterling, and B. P. Flannery, *Numerical Recipes in C: The Art of Scientific Computing*, 2nd ed. (Cambridge University Press, Cambridge, 1992).
- [3] S. L. Shapiro and S. A. Teukolsky, *Black Holes, White Dwarfs, and Neutron Stars: The Physics of Compact Objects* (Wiley, New York, 1983).

- [4] L. I. Petrich, S. L. Shapiro, and S. A. Teukolsky, *Phys. Rev. D* **31**, 2459 (1985).
- [5] S. L. Shapiro and S. A. Teukolsky, *Phys. Rev. D* **45**, 2739 (1992).
- [6] See, e.g., Figure 60, p. 322 of Ref. [1], and also C. W. Misner, K. S. Thorne, and J. A. Wheeler, *Gravitation* (Freeman, San Francisco, 1973), Figure 34.6, p. 924.
- [7] A. M. Abrahams, G. B. Cook, S. L. Shapiro, and S. A. Teukolsky, preprint CRSR 1051, Cornell University (1993).

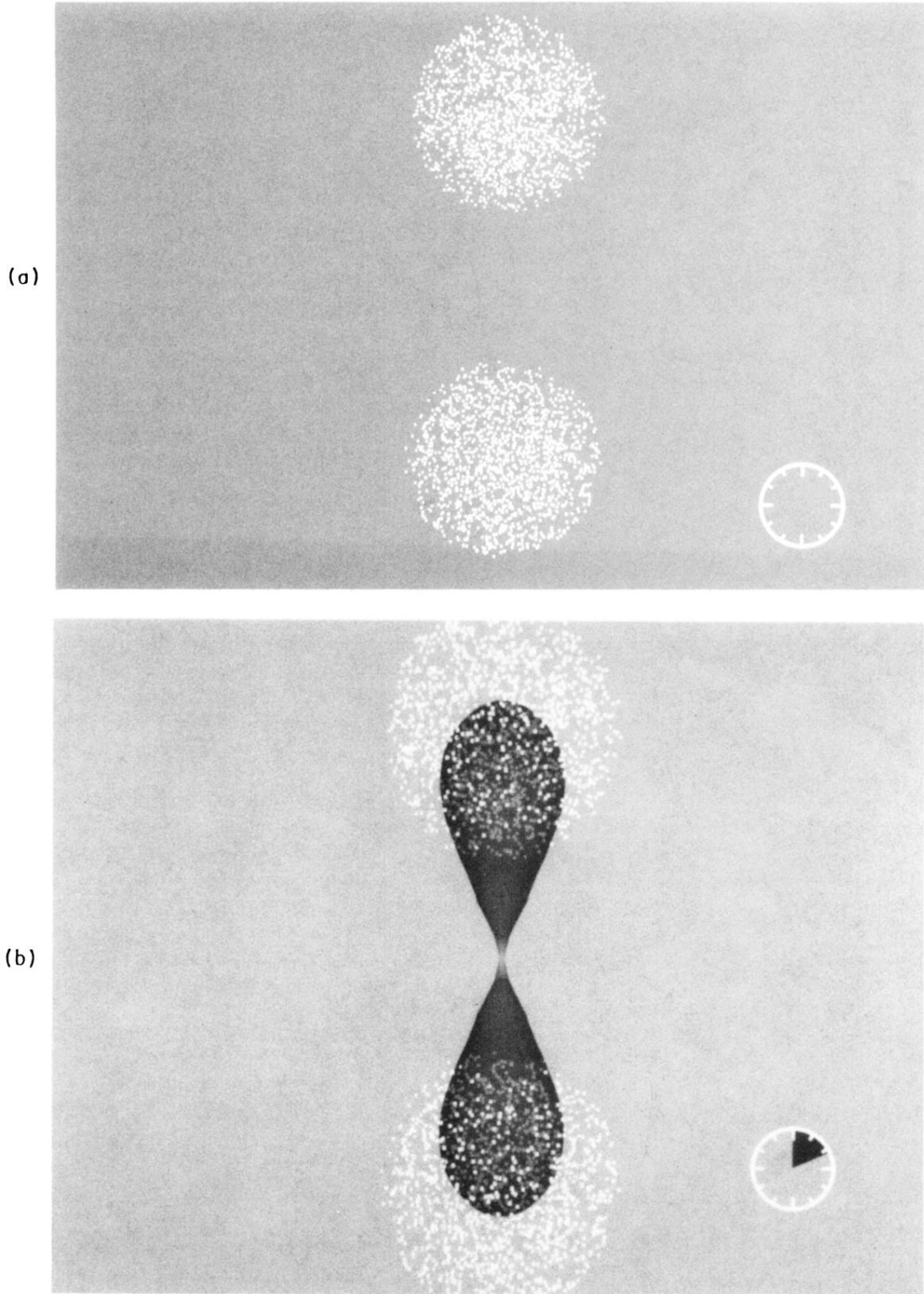
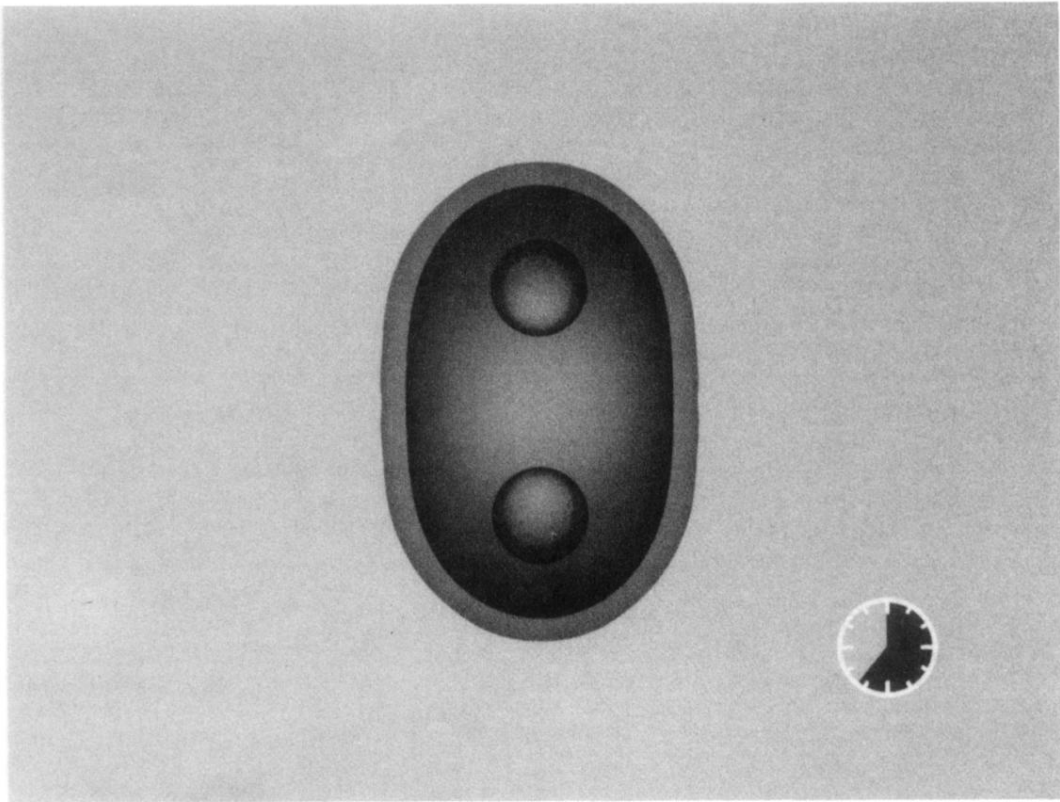


FIG. 1. Three-dimensional views of the head-on collision of boosted spherical clusters [5]. (a) Initial data. Each sphere has an initial radius $a/M=0.8$, an inward boost velocity $v=0.15$, and their centers are at $z_0/M=\pm 1.4$. Sample particles from the collisionless matter distribution are represented by white dots. A clock displaying the elapsed fraction of the total evolution time appears in the corner. (b) Horizon coalescence. At time $t/M=2.18$, the two event horizons coalesce (shaded hourglass). The clusters' centers are at $z/M=\pm 1.07$. The scale of the image has been enlarged by about a factor of 2 from that of (a). (c) Appearance of apparent horizons. At time $t/M \simeq 6.5$, the common apparent horizon appears, well inside the event horizon. At time $t/M \simeq 7.1$ (shown here), the disjoint apparent horizons appear. The outer shaded region denotes the event horizon, the darker shaded region just inside is the common apparent horizon, and the two darkest regions are the disjoint apparent horizons. (d) Final state. The event and common apparent horizons have settled down to a quasistationary state and coincide. At time $t/M \simeq 11.7$ shown here, the area is $\mathcal{A}/16\pi M^2=1.1$, the polar circumference is $\mathcal{C}_{\text{pole}}/4\pi M=1.1$, and the equatorial circumference is $\mathcal{C}_{\text{eq}}/4\pi M=1.0$.

(c)



(d)

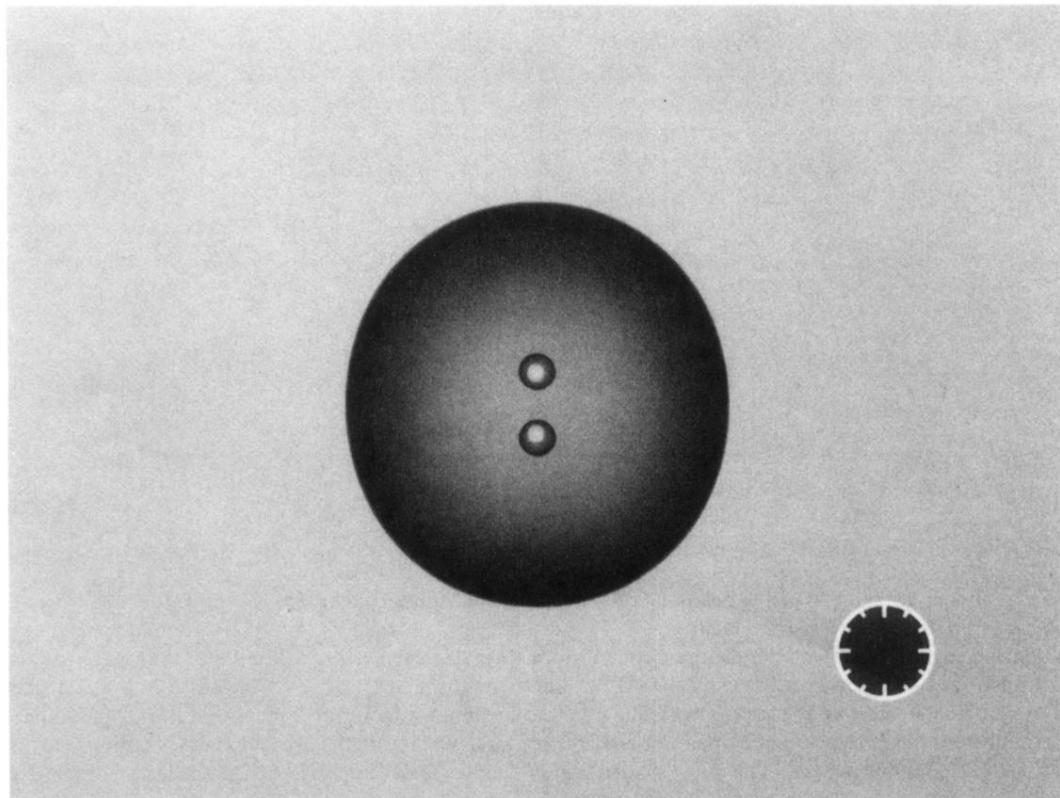


FIG. 1. (Continued).

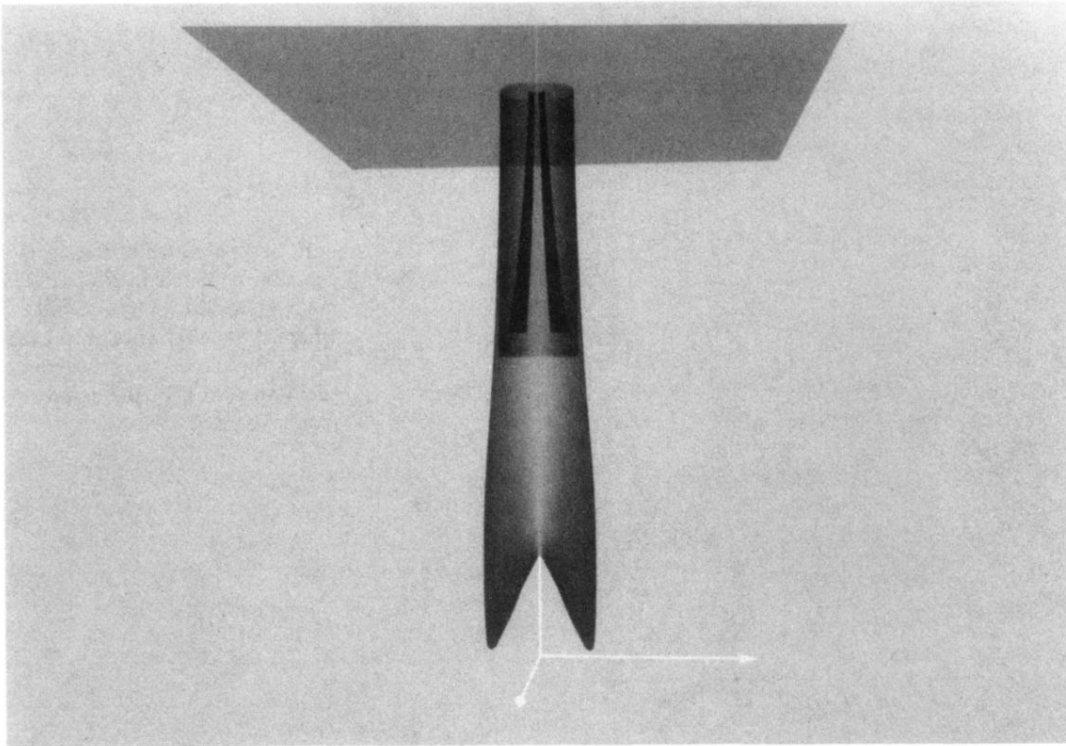


FIG. 3. Spacetime diagram for the collision depicted in Fig. 1. The time axis is vertical, the z axis (symmetry axis) points to the right, while the x axis (equatorial axis) points out of the page. The formation of the common and disjoint apparent horizons at $t/M \simeq 6.5$ and 7.1 , respectively, is seen as the sudden appearance of darker surfaces inside the event horizon (outermost shaded surface). The final hypersurface $t/M \simeq 11.7$ is shown as the plane at the top.

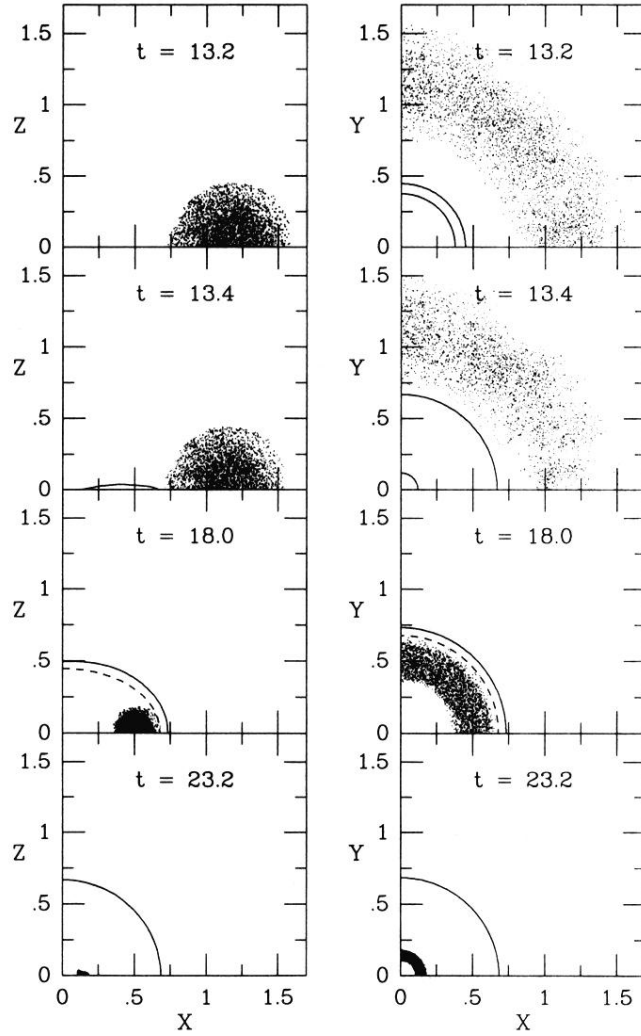


FIG. 6. Snapshots at selected times of the collapse of a rotating toroid of collisionless matter (case 10 of Ref. [7]). The left panel displays meridional slices, the right panel shows the equatorial plane. The solid line denotes the event horizon, the dashed line the apparent horizon. The earliest times shown are soon after the toroidal event horizon appears. By the final time shown, the event and apparent horizons coincide. t , x , y , and z are in units of M .

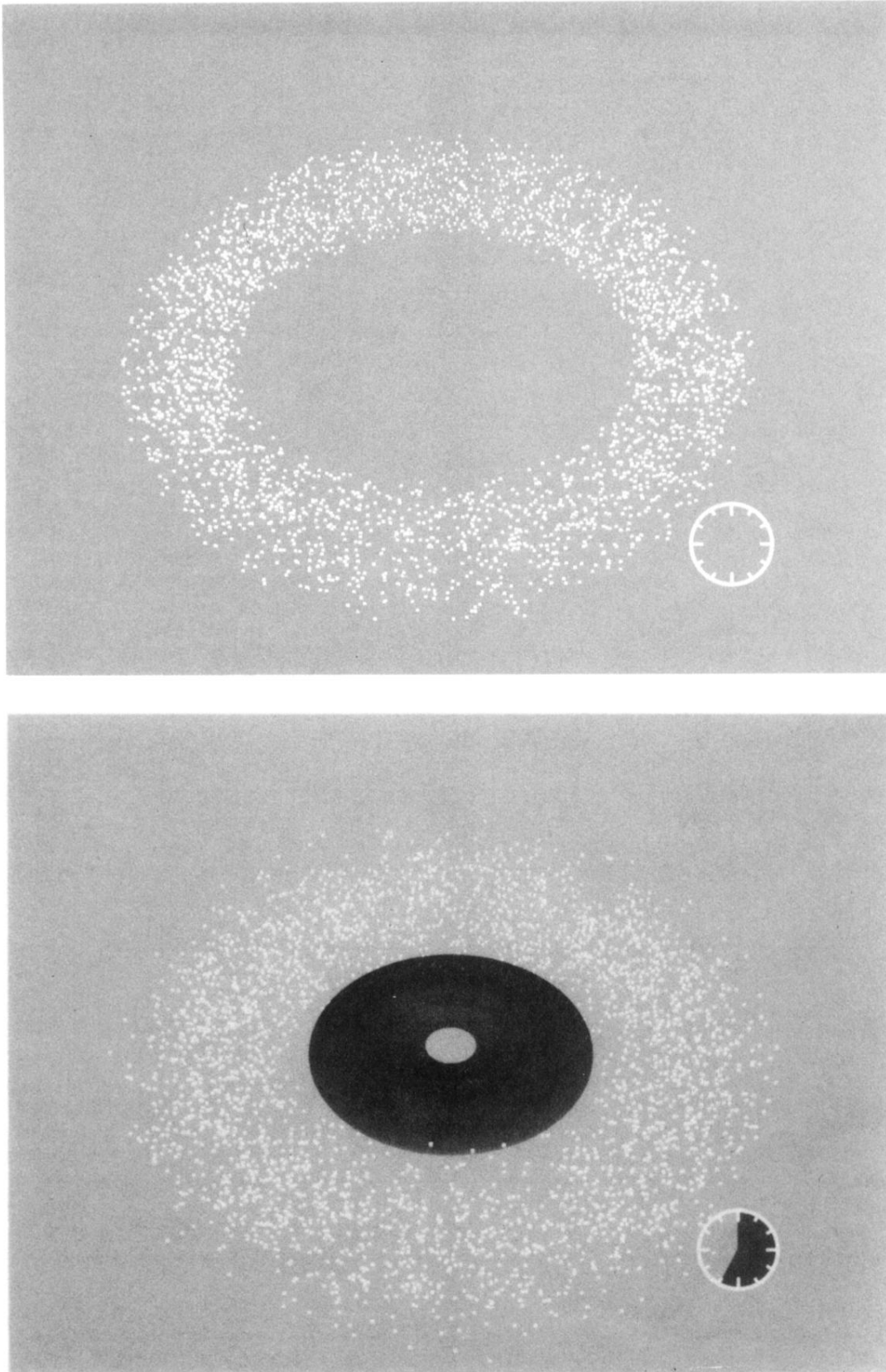


FIG. 7. Three-dimensional views of the collapse of the rotating toroid depicted in Fig. 6. The images are viewed from 45° above the equatorial plane. The first image shows the initial configuration, while the remaining three images are at the same times as the last three images of Fig. 6. The outermost shaded region is the event horizon, the shaded region inside it is the apparent horizon. The scale of the last three images has been enlarged by about a factor of 2 over the first image.

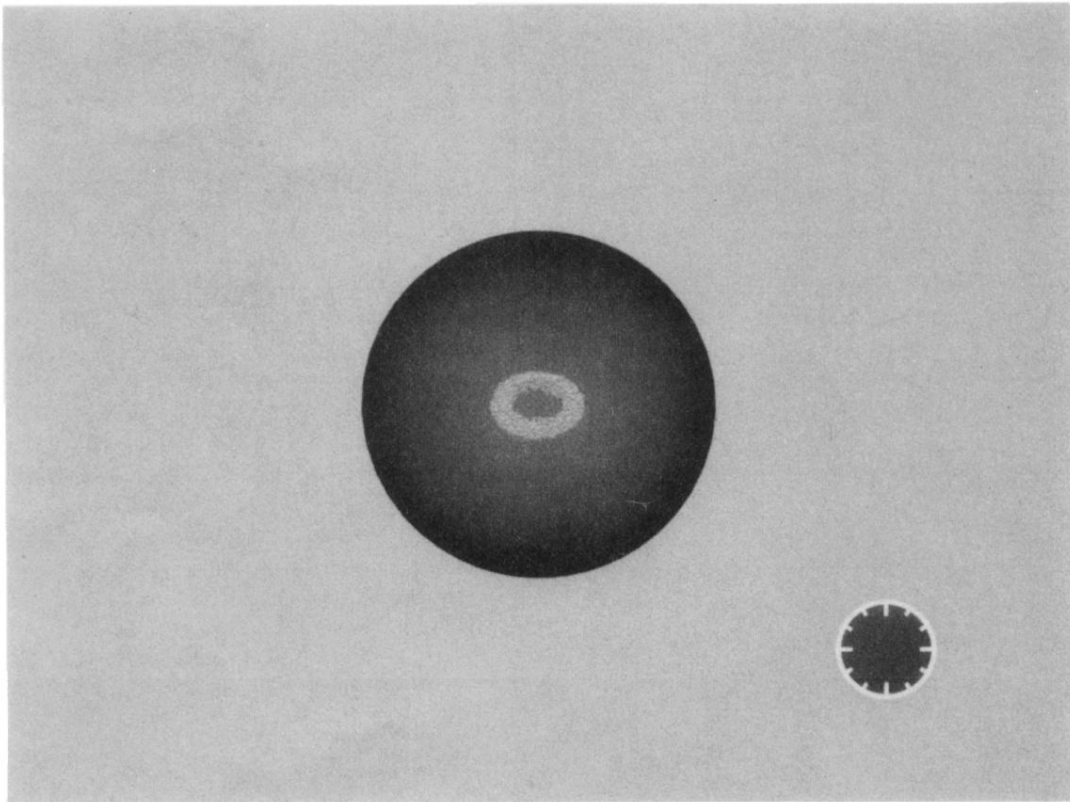
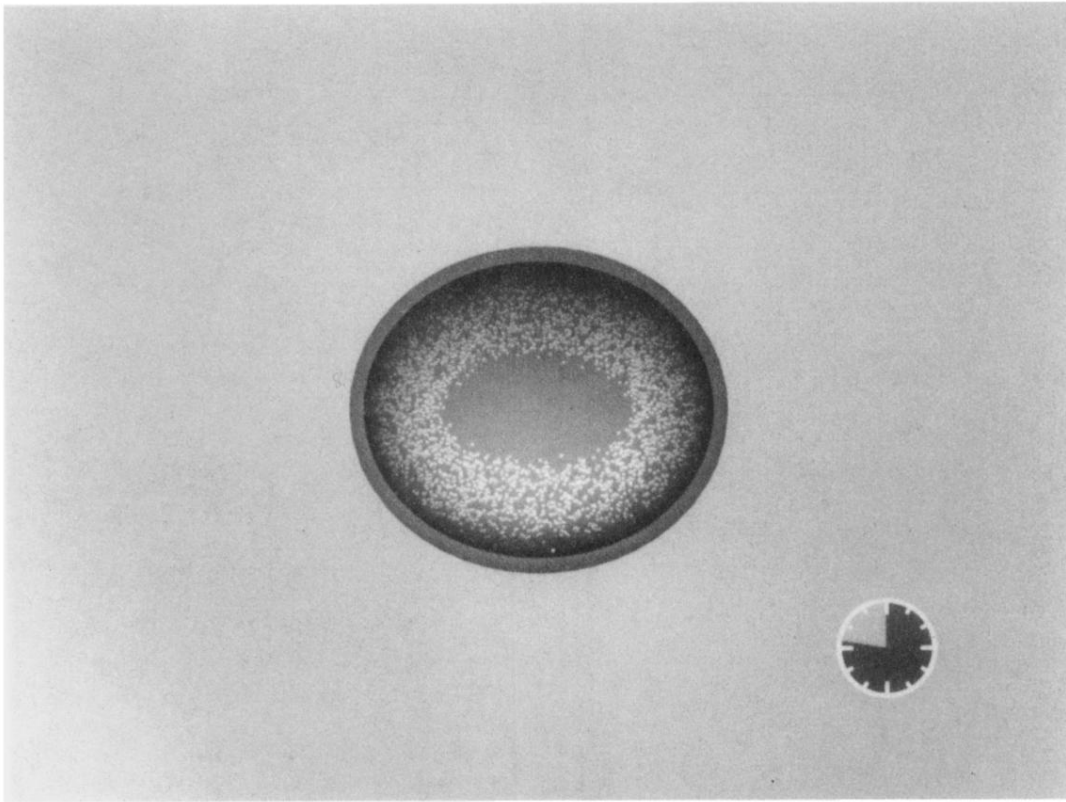


FIG. 7. (Continued).